Rearrangement of a unique Kv1.3 selectivity filter conformation upon binding of a drug

Anu Tyagi[a] , Tofayel Ahmed[b], Shi Jian[c], Saumya Bajaj[a,d], Seow Theng Ong[d] , Stephanie Shee Min Goay[d], Yue Zhao[e], Igor Vorobyov[f,g] , Changlin Tian[e], K. George Chandy[d] , and Shashi Bhushan[a,h,1]

[a]School of Biological Sciences, Nanyang Technological University, Singapore 637551; [b]Department of Structural Biology, Max Planck Institute of Biophysics, 60438 Frankfurt am Main, Germany; [c]Department of Biological Sciences, National University of Singapore, Singapore 117557; [d]LKCMedicine-ICESing Ion Channel Platform, Lee Kong Chian School of Medicine, Nanyang Technological University Singapore, Singapore 636921; [e]Hefei National Laboratory of Physical Sciences at Microscale and School of Life Sciences, University of Science and Technology of China, Hefei, 230026, China; [f]Department of Physiology and Membrane Biology, University of California, Davis, CA 95616; [g]Department of Pharmacology, University of California, Davis, CA 95616; and [h]Nanyang Institute of Structural Biology, Nanyang Technological University, Singapore 639798

We report two structures of the human voltage-gated potassium channel (Kv) Kv1.3 in immune cells alone (apo-Kv1.3) and bound to an immunomodulatory drug called dalazatide (dalazatide–Kv1.3). Both the apo-Kv1.3 and dalazatide–Kv1.3 structures are in an activated state based on their depolarized voltage sensor and open inner gate. In apo-Kv1.3, the aromatic residue in the signature sequence (Y447) adopts a position that diverges 11 Å from other K+ channels. The outer pore is significantly rearranged, causing widening of the selectivity filter and perturbation of ion binding within the filter. This conformation is stabilized by a network of intrasubunit hydrogen bonds. In dalazatide–Kv1.3, binding of dalazatide to the channel's outer vestibule narrows the selectivity filter, Y447 occupies a position seen in other K+ channels, and this conformation is stabilized by a network of intersubunit hydrogen bonds. These remarkable rearrangements in the selectivity filter underlie Kv1.3's transition into the drug-blocked state.

ion channels | potassium channels | selectivity filter | ShK | dalazatide

Potassium channels form K+-selective pores that span cell membranes in virtually all living organisms. In humans, a family of 78 genes encodes four classes of K+ channels (voltage-gated, calcium-activated, inward rectifier, and two-pore channels), which are involved in a multitude of physiological functions in both electrically excitable and nonexcitable cells (1). All four classes of channels conduct K+ ions selectively and rapidly, but they differ in how they are gated. The selectivity filter is the structural element responsible for the exquisitely K+-selective pore (2–5). It is the narrowest part of the ion conduction pathway and connects a water-filled cavity in the center of the protein with an outer vestibule in the extracellular solution. The filter accommodates K+ ions at four sites called S1, S2, S3, and S4 starting at the extracellular side. The signature sequence G(Y/F)G in the selectivity filter plays a critical role in making the pore K+ selective (6, 7). In all K+ channel structures determined, both bacterial and eukaryotic, the aromatic residue (Y or F) in the signature sequence is nearly identical in position, although these channels differ in the conformation (closed or open) of the S6 helical inner gate (8). In the hERG/ Kv11.1 channel, a subtle deviation in the position of F627 in the signature sequence causes a slight widening of the selectivity filter, which has been suggested to underlie the channel's transition into the C-type inactivated state (8).

The voltage-gated potassium channel (Kv) Kv1.3–Kvβ2 in lymphocytes and microglia provides the counterbalancing cation efflux to promote calcium entry necessary for calcium signaling (9, 10). Selective blockers of Kv1.3–Kvβ2 treat diverse autoimmune and neuroinflammatory diseases in rodent models (9, 10), highlighting the channel's physiological and pharmacological importance. Here, we determined structures of Kv1.3 complexed to its accessory subunit Kvβ2 alone (apo-Kv1.3) and

bound to dalazatide (dalazatide–Kv1.3), a potent and selective peptide inhibitor of Kv1.3 in clinical trials for autoimmune and neuroinflammatory diseases (10–14). Both apo-Kv1.3 and dalazatide–Kv1.3 are in the activated state based on the depolarized voltage sensor and open S6 helical inner gate. Comparison of the two structures reveals substantial conformational changes in the selectivity filter. In apo-Kv1.3, Y447 in the signature sequence diverges more than 11 Å from the position of corresponding aromatic residues in other K+ channels, both in eukaryotes and bacteria. The outer pore is wider at S1 and S2 and narrowed at S0 K+-binding sites, resulting in loss of the K+ ion from site S2. A network of intrasubunit hydrogen bonds (H451–Y447, H451–D449) stabilizes this unique conformation of the selectivity filter of apo-Kv1.3, and, interestingly, the intrasubunit hydrogen bond (W436–D449) that prevents C-type inactivation (15) is absent. Apo-Kv1.3's selectivity filter and voltage-sensing domain (VSD) differ significantly from two structures of Kv1.3 that were recently described (16). In dalazatide–Kv1.3, dalazatide's interaction with H451 disrupts the H451–Y447 hydrogen bond, freeing Y447 to swing back into the interior of the selectivity filter and adopt a position seen in other K+ channels. The selectivity filter is narrower, and K+ ions are present at sites S2–S4 but not at S1. This

Significance

Voltage-gated potassium channels (Kv) open with membrane depolarization and allow the flow of K+ ions. Ion flow is tightly governed by time-dependent entry into nonconducting inactivated states. Here, we focus on Kv1.3, a channel of physiological importance in immune cells. We used cryogenic electron microscopy to determine structures of human Kv1.3 alone and bound to dalazatide, a peptide inhibitor in human trials. In the unbound state, Kv1.3's outer pore is rearranged compared to all other K+ channels analyzed. Interaction of dalazatide with Kv1.3's outer pore causes a dynamic rearrangement of the selectivity filter as Kv1.3 enters a drug-blocked state.

conformation is stabilized by a network of intersubunit hydrogen bonds (Y447–W437, Y447–T441, and H451–D449), but the intrasubunit hydrogen bond (W436–D449) that prevents C-type inactivation (15) is likely absent. Our structures provide a basis for the design of Kv1.3 inhibitors for use as immunomodulatory therapeutics.

Results and Discussion

Structure of the Human Kv1.3–Kvβ2.1 Complex (Apo-Kv1.3). Human and rodent Kv1.3 exhibit identical biophysical properties (17, 18) even though the human sequence (accession no. NP_002223) contains an additional 52 residues at the N terminus. Human Kv1.3 lacking these 52 residues exhibits biophysical properties matching those of native Kv1.3 in human T lymphocytes (16, 17). For structural studies, we coexpressed human Kv1.3 lacking the first 52 residues with its accessory subunit Kvβ2.1 in Sf9 insect cells and purified the Kv1.3–Kvβ2 complex (*SI Appendix*, Fig. S1). Two-dimensional (2D) class averages from negative-stained particles of the purified complex revealed clear side views of the channel surrounded by a disk-shaped detergent micelle to which Kvβ2 was anchored (*SI Appendix*, Fig. S2). The Kv1.3–Kvβ2 complex was frozen on R1.2/1.3 holey cryo-grids with and without a homemade 2-nm ultrathin (UT) carbon support film. Two different data sets, one each for holey and carbon support films, were acquired on a 300-kV Titan Krios using a Gatan K3 direct detection camera. However, both datasets failed to produce high-resolution three-dimensional (3D) electron microscopy (EM) maps because the particles adopted mainly side views with some oblique views and a paucity of top/bottom views. After screening different buffer and grid types, we found that adding 0.01% lauryldimethylamine N-oxide (LDAO) detergent to our standard buffer (20 mM HEPES, pH 7.5, 150 mM KCl, and 0.05% glycodiosgenin [GDN]) and using the UT carbon support film with Quantifoil R1.2/1.3 cryo-grids mitigated the preferred orientation problem. Kv1.3–Kvβ2 particles frozen on a UT carbon support film in the presence of LDAO revealed 2D class averages displaying multiple views with detailed secondary structures resolved both in the cytosolic and membrane domains (*SI Appendix*, Fig. S3). A total of 321,674 particles were selected after several rounds of 2D and 3D classification with Relion (19). The resulting 3D map was resolved to a 3.1-Å resolution (*SI Appendix*, Fig. S4). While the cytosolic regions including Kvβ2 and the soluble tetramerization domain (T1) of Kv1.3 were well resolved, the map displayed a lower resolution in the transmembrane region. To improve resolution, the density outside of the transmembrane region was subtracted using a soft mask around the detergent micelle (*SI Appendix*, Fig. S4) followed by 2D and 3D classification. A total of 177,130 signal-subtracted particles produced a 3D map of the transmembrane region resolved to 3.4 Å with C4 symmetry applied and 3.9 Å without any symmetry imposed (*SI Appendix*, Fig. S4). Local resolution varied from 3 to 5 Å in the C4 map with most of the region resolved to about 3 Å (*SI Appendix*, Fig. S5 and Table S1).

Individual signal-subtracted C4 maps for the transmembrane region and the region encompassing T1 domains and Kvβ2 subunits were used to build models, which were then combined. A total of 358 Kv1.3 residues between Q99 and L204 (N-terminal region spanning the T1 domain), E208 and R260 (distal N terminus to the proximal S1–S2 loop), S289 and G352 (distal S1–S2 loop to the end of the S3 helix), and S359 and G493 (end of the S3–S4 loop to the proximal C terminus) were modeled. The Kvβ2 model contains 328 residues between R34 and S361. In each of the four subunits, the map also contains nonprotein densities in the transmembrane region that resemble a pair of phospholipids, three cholesteryl hemisuccinate molecules, and three acyl tails of bulk lipids. The model of the transmembrane region was fitted into the complete map to obtain a model of the entire apo-Kv1.3 (Kv1.3–Kvβ2) complex (Fig. 1 A

and B). The density of bound NADP$^+$, which is required for the oxidoreductase activity of Kvβ2, is clearly resolved (Fig. 1C). Side chain densities are visible for most transmembrane helices, the pore helix, and the selectivity filter residues (Fig. 1D and *SI Appendix*, Fig. S6). The transmembrane segments of Kv1.3 are domain swapped so that the VSD of one subunit interacts with the S5 helix of a neighboring subunit (Fig. 1A). The S6 helical inner gate is in the open conformation (*SI Appendix*, Fig. S7). In the VSD, side chain densities of the six positively charged amino acids in the S4 helix (R364, R367, R370, R373, K376, and R379) and the three residues in the charge transfer center (F306, E309, and D332) are well defined (Fig. 1D and *SI Appendix*, Fig. S6). The six positively charged amino acids in the S4 helix are labeled R1, R2, R3, R4, K5, and R6 in Fig. 1 F and G. The charge transfer center functions as a fulcrum along which positively charged residues in the S4 helix slide in response to changes in membrane potential. In apo-Kv1.3, K5 is at the level of F306, and R1 and R2 are close to the extracellular surface of the channel (Fig. 1F), consistent with the VSD being fully depolarized. The depolarized voltage sensor and open S6 helical inner gate indicates that apo-Kv1.3 is in the activated state. Superimposition of our model of apo-Kv1.3 with the transmembrane regions of the rat Kv1.2–Kv2.1 paddle chimera (KvChim) (Protein Data Bank [PDB]: 2R9R) (20) shows good alignment in the VSD, but structural differences are clearly visible in the pore region and particularly in the selectivity filter (Figs. 1 B, E, and F and 2). Apo-Kv1.3 shows overall similarity with the model of a recently determined Kv1.3 structure (PDB: 7EJ1) (16) (referred to hereafter as Kv1.3-7EJ1) (*SI Appendix*, Fig. S8), but differences were observed in the VSD (Fig. 1G) and the selectivity filter (Fig. 2). In the VSD of Kv1.3-7EJ1, side chain densities are not visible in the EM map (Electron Microscopy Data Bank [EMDB]: 31148) (16) for R1, R2, R4, K5, and R6 residues in the S4 helix and F306, E309, and D332 in the charge transfer center; yet in the model, R4 is positioned at the charge transfer center (Fig. 1G).

Conformation of the Selectivity Filter. We aligned amino acid sequences of the pore region of Kv1.3 with the four K$^+$ channels (KvChim, hERG/Kv11.1, Eag-1/Kv10.1, and KcsA) that we used for structural comparisons (Fig. 2A). KvChim (PDB: 2R9R) is a closely related channel with its S6 helical inner gate open (20), hERG/Kv11.1 (PDB: 5VA1) is a distantly related channel in an open conformation (8), rat Eag-1/Kv10.1 (PDB: 5K7L) is a distantly related channel in a closed conformation (21), and bacterial KcsA (PDB: 1K4C) is a very distantly related bacterial channel in a closed conformation (5). Despite differing in the conformational state of the inner gate, these four channels are nearly identical with respect to the position of the aromatic residue (Y or F) in the signature sequence (8). The selectivity filter of apo-Kv1.3 is significantly different from these channels. Fig. 2B shows EM density fitted to the model of apo-Kv1.3's selectivity filter. Based on EM densities in the apo-Kv1.3 pore, we modeled K$^+$ ions at sites S1, S3, and S4, but S2 was empty (Fig. 2B and *SI Appendix*, Fig. S9). The three "in-filter" ions appear to be equidistant, and, given the significant rearrangements at G446–Y447–G448, it is possible that the expected S1–S2 coordination sites have changed, and a new site has been generated (S*), which now coordinates a single ion. In the central cavity below the selectivity filter, we observed additional density in maps generated with both C4 and C1 symmetry (*SI Appendix*, Fig. S9) into which we could build a partially hydrated K$^+$ ion (Fig. 2B). We refer to this site as S$_{cav}$ (Fig. 2B). A fully hydrated K$^+$ ion is present in the central cavity of KcsA (5), but this site is further away from the selectivity filter than S$_{cav}$ in Kv1.3 (*SI Appendix*, Fig. S10). Ordered water is present in the central cavity (*SI Appendix*, Figs. S9 and S10) possibly to facilitate the passage of K$^+$ ions from the cytoplasm to the selectivity filter.
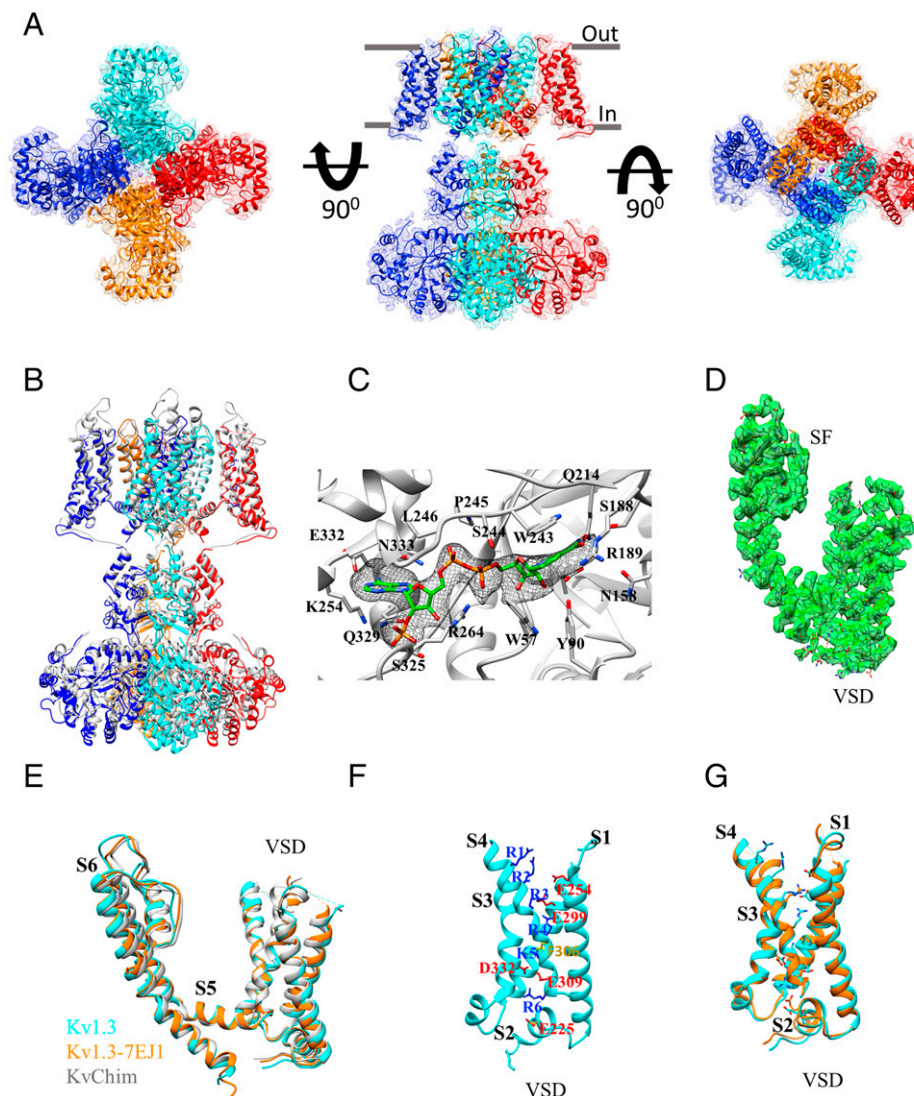
Fig. 1. Structure of the human Kv1.3–Kvβ2 complex (apo-Kv1.3). (*A*) Cryo-EM density map of Kv1.3–Kvβ2 with a fitted model viewed from the membrane plane (*Center*), from inside the cell (*Left*), and from the extracellular side (*Right*). (*B*) Superposition of Kv1.3–Kvβ2 with KvChim (PDB: 2R9R, gray). Each subunit of Kv1.3–Kvβ2 is colored differently. (*C*) Binding pocket of NADP+ in Kvβ2. The density of NADP+ is shown in gray mesh with surrounding residues in Kvβ2 labeled. (*D*) Density of the transmembrane region of one subunit of Kv1.3 fitted with the model. Voltage-sensing domain (VSD) and selectivity filter region (SF) are labeled. (*E*) Superposition of the model in *D* (cyan) with the corresponding regions of KvChim (gray) and Kv1.3-7EJ1 (orange). (*F*) Model of the VSD of apo-Kv1.3 with positively charged residues in the S4 helix and charge center residues labeled. (*G*) Superposition of VSD of apo-Kv1.3 (cyan) with Kv1.3-7EJ1 (orange).

Since Kv1.3 and KvChim are closely related, we compared their selectivity filters. For our comparison, we used the high-resolution X-ray structure of KvChim in detergent in the presence of lipids (PDB: 2R9R). In this structure, the voltage sensors are in a depolarized position, the inner gate is open, and all four K^+-binding sites in the selectivity filter are occupied, suggesting that the channel is in an open conducting conformation (20). Apo-Kv1.3's selectivity filter is wider than KvChim at K^+-binding sites S1 and S2 and narrower at site S0 (Fig. 2*C* and *SI Appendix*, Fig. S11*A*). The carbonyl groups of residues G446 and Y447, which are involved in the coordination of K^+ ions at S1 and S2, are pointed away from the selectivity filter (Fig. 2*C*). Due to these structural changes, coordination of K^+ at S2 is lost, resulting in no density observed for K^+ in the EM maps (Fig. 2*B* and *SI Appendix*, Figs. S9 and S10). The two channels show similar geometry at sites S3 and S4, and the partially hydrated K^+ at S_{cav} in Kv1.3 is not present in KvChim (Fig. 2*C* and *SI Appendix*, Fig. S11*A*). This pattern of K^+ occupancy

in the selectivity filter is similar to the cryo-electron microscopy (cryo-EM) structure of KvChim in lipid nanodiscs (PDB: 6EBK; EMDB: 9024) (22).

The widened selectivity filter and the absence of K^+ from site S2 (Fig. 2 *B* and *C*) is due to the side chain of Y447 in apo-Kv1.3's signature sequence, well defined in the maps (Fig. 2*B* and *SI Appendix*, Figs. S6 and S9), adopting a position significantly different (11 Å) from aromatic residues in the signature sequences of KvChim, hERG, Eag-1, and KcsA (Fig. 2 *A* and *D*). Y447's new position is stabilized by its interaction with H451 (Fig. 2 *A* and *E*), a residue at the external entrance to the pore (23–25). H451 is 3.6 Å from Y447 and 3.8 Å from D449 in the same subunit (Fig. 2 *E* and *F*). The map shows that the densities around H451–Y447 and H451–D449 are connected (Fig. 2 *B*, *E*, and *F*), suggesting possible intrasubunit interactions between H451 and Y447 as well as H451 and D449 residues. In other K^+ channels, a network of intrasubunit and intersubunit hydrogen bonds stabilizes the outer pore (15, 22,
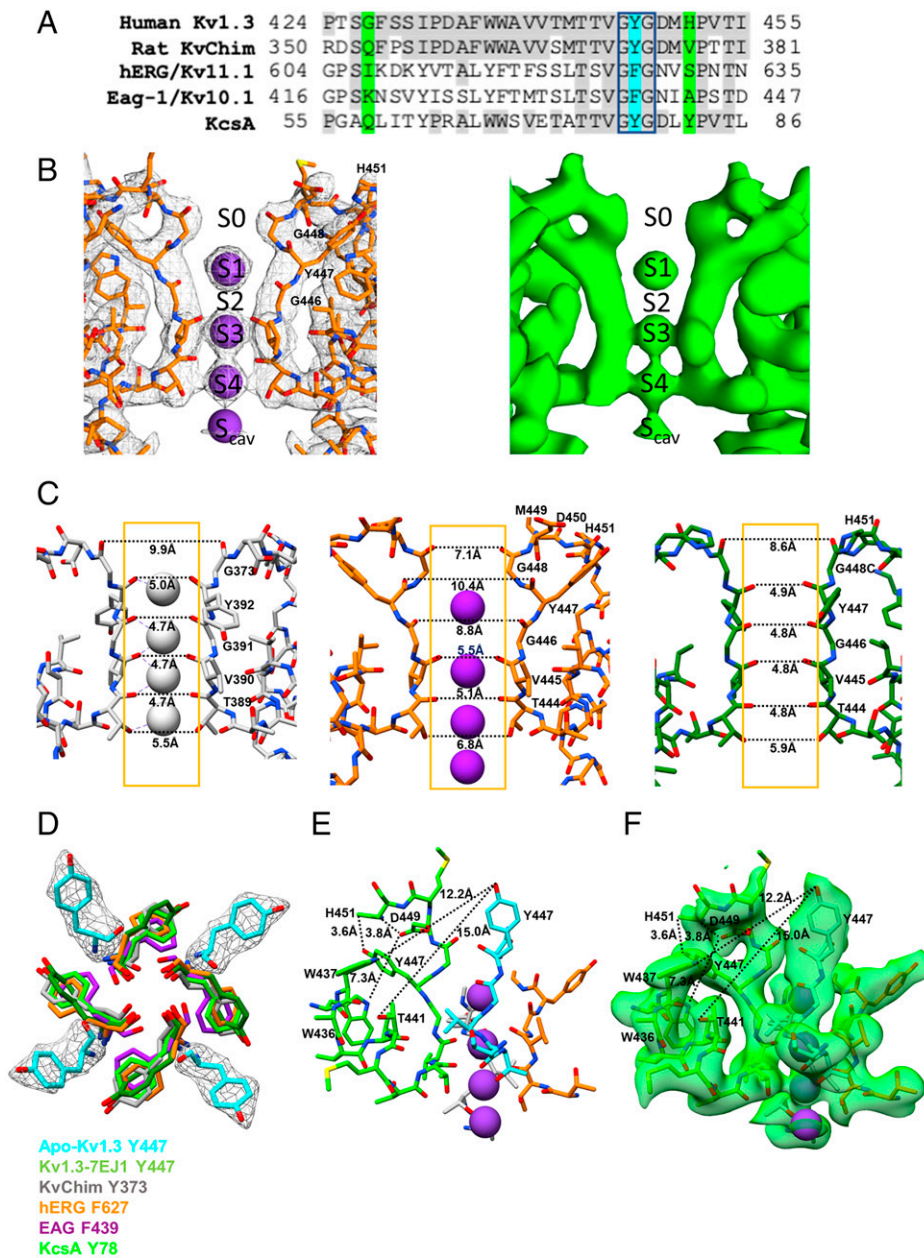
Fig. 2. Selectivity filter of apo-Kv1.3. (*A*) Sequence alignment of the pore region of human Kv1.3 (accession number NP_002223) with KvChim (PDB: 2R9R), hERG/Kv11.1 (PDB: 5VA1), rEag-1/Kv10.1 (PDB: 5K7L), and bacterial KcsA (PDB: 1K4C). Identical residues are shaded in gray. The signature sequence G[Y/F]G is boxed, and the aromatic residue is highlighted in blue. Two residues in the outer vestibule (G427, His451) in Kv1.3 are highlighted in green. (*B*) Side view of EM density of the Kv1.3–Kvβ2 map in white mesh with fitted model (*Left*) and surface in green (*Right*). The signature sequence is labeled. K$^+$ ions (purple spheres) are seen at S1, S3, S4, and S$_{cav}$; the K$^+$ ion is missing at site S2. (*C*) Models of the selectivity filter of KvChim (PDB: 2R9R) (*Left*), apo-Kv1.3 (*Middle*), and Kv1.3-7EJ1 (PDB: 7EJ1) (*Right*). Distances between the carbonyl O atom of the selectivity filter residues are shown with two subunits displayed for clarity. (*D*) Overlay of Y447-apo-Kv1.3 (cyan) with equivalent aromatic residues in the selectivity filter (shown as sticks) of Y373-KvChim (gray), F627-hERG (orange), F439-Eag-1 (purple), Y78-KcsA (neon green), and Y447-Kv1.3-7EJ1 (olive green). EM density of Y447-apo-Kv1.3 in white mesh is overlapped with the model (cyan). (*E* and *F*) Model of the outer pore of apo-Kv1.3 with individual subunits colored cyan, green, gray, and orange (*E*) and with the density in translucent green surface (*F*). Distances are shown between H451 and Y447 (3.6 Å), H451 and D449 (3.8 Å), and W436 and D449 (7.3 Å) in the same subunit, and W437 and Y447 (12.3 Å) and Y447 and T441 (15 Å) in adjacent subunits. Only selected residues are shown for clarity.

26, 27). The network in KvChim (PDB: 2R9R) (20) includes intrasubunit (W362–D375) and intersubunit (W363–Y373; S367–Y373) hydrogen bonds (*SI Appendix*, Fig. S11*B*) (22, 26, 27). The equivalent intrasubunit (W434–D447) hydrogen bond in the Shaker Kv channel prevents C-type inactivation (15). In apo-Kv1.3, the corresponding residues (Fig. 2*A*) are too far from each other to form intrasubunit (W436–D449 = 7.3 Å) and intersubunit (W437–Y447 = 12.3 Å; Y447–T441 = 15 Å) hydrogen bonds (Fig. 2 *E* and *F*). A network of intrasubunit

(H451–Y447 and H451–D449) hydrogen bonds stabilizes this conformation of the selectivity filter of apo-Kv1.3.

The conformation of apo-Kv1.3 was not observed in two recently determined structures of Kv1.3 (16). Based on the lack of K$^+$ at ion-binding site S2 and its similarity to KvChim-nanodisc (PDB: 6EBK) (*SI Appendix*, Fig. S12), Kv1.3-7EJ1 was suggested to be in the C-type inactivated state (16). However, in Kv1.3-7EJ1, the outer pore is not widened (Fig. 2*C*), Y447's position is like that in KvChim (Fig. 2*D* and *SI*

Appendix, Figs. S12–S14), and the intrasubunit W436–D449 hydrogen bond that prevents C-type inactivation is present based on molecular dynamics simulation (MDS) studies (16). The rapidly inactivating H451N mutant of Kv1.3 (PDB: 7EJ2; EMDB: 31149) did exhibit a widened selectivity filter (at S0, S1, and S2), site S2 lacked a K$^+$ ion, and the critical W436–D449 hydrogen bond was missing, but the rearrangement of Y447 and D449 was not observed (*SI Appendix*, Fig. S12). In these two structures, missing or weak side chain densities in the EM density maps (EMDB: 31148/PDB: 7EJ1; EMDB: 31149/PDB: 7EJ2) for many critical residues in the pore domain and selectivity filter may have precluded visualization of the unique conformation of apo-Kv1.3 (Figs. 1 *G* and 2 *D* and *E* and *SI Appendix*, Figs. S8, S12, and S14). In all Kv structures determined by cryo-EM at about 4-Å resolution, the density for Y447 and its equivalent aromatic residues in the selectivity filter have been visualized in EM density maps. However, the density for Y447 is missing in EM density maps for both Kv1.3-7EJ1 and H451N-Kv1.3 (*SI Appendix*, Fig. S12), which makes comparisons of these structures with apo-Kv1.3 less reliable.

Interestingly, a recent cryo-EM study of the Shaker-IR (fast inactivation removed) channel in lipid bilayers revealed that the selectivity filter of the rapidly inactivating W434F mutant was significantly wider than the wild-type channel due to a drastic reorientation of Y445 away from the interior of the selectivity filter (28). Most importantly, the conformation of the selectivity filter of W434F Shaker-IR (28) is similar to the conformation of apo-Kv1.3. Based on MDS studies, the W434F mutant was suggested to be in a nonconducting C-type inactivated state (28). We suggest that apo-Kv1.3 maybe in the C-type inactivated state because of the similarity of the unique conformation of its selectivity filter with that of Shaker-IR W434F and because of the absence of K$^+$ from site S2, dilation of apo-Kv1.3's selectivity filter at S1 and S2, and absence of the intrasubunit hydrogen bond (W436–D449) that prevents C-type inactivation (15).

Structure of Dalazatide–Kv1.3 (Dalazatide Bound to Kv1.3–Kvβ2). A plethora of cysteine-rich peptides from venomous creatures (scorpions, sea anemones, and snakes) target the outer pore vestibule region of Kv1.3 with nanomolar and subnanomolar affinity (11). These peptides make multiple interactions with the outer vestibule region of Kv1.3 and occlude the selectivity filter with a positively charged residue. Solid-state NMR studies on a Kv1.3–KcsA chimera grafted with Kv1.3's outer vestibule revealed that binding of kaliotoxin from scorpion venom caused profound conformational changes in the external selectivity filter of the channel, including a large shift in the position of Y78 (the residue equivalent to Y447 in Kv1.3) (29, 30) Follow-up all-atom MDS studies coupled with solid-state NMR and electrophysiological measurements revealed that kaliotoxin-induced conformational changes in KcsA–Kv1.3 were structurally and functionally related to recovery from C-type inactivation (30). Further, electrophysiological experiments revealed that C-type inactivation reduced the affinity of kaliotoxin for Kv1.3 due to decreased toxin binding to the inactivated conformation (30). In contrast, electrophysiological studies on the Shaker-IR channel suggest that binding of toxins (charybdotoxin and κ-conotoxin-PVIIA) does not alter the conformation of the outer selectivity filter, and inactivation does not alter the affinity of toxins for that channel (31). These results suggest that outer pores of Kv1.3–KcsA and Kv1.3 respond differently to the binding of toxins than Shaker-IR. Kv1.3 also differs from Shaker-IR and KvChim in exhibiting cumulative inactivation (current amplitude decreases with repeated depolarizing pulses) due to its slow recovery from C-type inactivation (9). Given these differences and given that apo-Kv1.3 might be in the C-type inactivated state for the reasons mentioned above, we wondered if

binding of a toxin would reconfigure the selectivity filter of apo-Kv1.3.

For these studies, we chose dalazatide/ShK-186 (9–13), a 37-residue synthetic derivative of stichodactyla toxin (ShK) from the sea anemone *Stichodactyla helianthus* (11, 12, 14). Dalazatide is a highly selective Kv1.3 inhibitor and the first in class to have entered human clinical trials for the treatment of autoimmune and neuroinflammatory diseases (13). Dalazatide binds to Kv1.3's outer vestibule, making multiple interactions with the channel, and it plugs the pore by inserting a positively charged residue into the selectivity filter (14, 32). During 200-ms depolarizing pulses (−80 mV to 40 mV) applied at 45-s intervals, dalazatide blocked Kv1.3 with picomolar potency (half-maximal inhibitory concentration [IC$_{50}$] = 19.2 ± 1.1 pM) (*SI Appendix*, Fig. S15 *A* and *B*). To determine whether dalazatide binds to the closed state of the channel, we applied a 200-ms depolarizing pulse (from a holding potential of −80 mV to 40 mV) to elicit a control Kv1.3 current, then perfused dalazatide (50 pM) into the bath while keeping the channel closed before pulsing again at 45-s intervals. Dalazatide blocked 65% of the Kv1.3 current at the first pulse after peptide incubation, and this blockade did not increase during a further nine depolarizing pulses (*SI Appendix*, Fig. S15 *C* and *D*). This result suggests that dalazatide binds to the closed state of Kv1.3 and does not exhibit use-dependent blockade of the channel. Next, we assessed if inactivation altered dalazatide's affinity for Kv1.3. We lengthened the pulse duration to increase C-type inactivation and compared block by dalazatide (50 pM) of Kv1.3 at different pulse durations (200, 1,000, and 2,000 ms) applied at 45-s intervals. Dalazatide was less effective in blocking Kv1.3 current (both peak and end-of-pulse current amplitude) during longer depolarizing pulses (*SI Appendix*, Fig. S15 *E–G*), suggesting that inactivation reduces the affinity of dalazatide for the channel. As a further test, we determined the IC$_{50}$ for dalazatide block during short (50-ms) and long (1,000-ms) pulses applied at 45-s intervals (*SI Appendix*, Fig. S15*H*). About a sevenfold shift in IC$_{50}$ was observed during the longer pulse (IC$_{50}$ at 50 ms = 4.9 ± 1 pM, *n* =15; IC$_{50}$ at 1,000 ms = 34.6 ± 1 pM, *n* = 8) (*SI Appendix*, Fig. S15*I*). Dalazatide's potency, selectivity, therapeutic potential, and interesting interactions with Kv1.3 make it an attractive peptide for this study.

We determined the structure of dalazatide–Kv1.3 to a resolution of 3.4 Å (Fig. 3*A* and *SI Appendix*, Figs. S16–S20 and Table S1). The dalazatide–Kv1.3 model contains 362 Kv1.3 residues between Q99 and L204 (N-terminal region spanning the T1 domain), E208 and S262 (distal N terminus to the proximal S1–S2 loop), and S290 and E490 (distal S1–S2 loop to the proximal C terminus), one phospholipid, one cholesteryl hemisuccinate molecule, and three acyl tails of bulk lipids in each subunit. The density for the external S3–S4 loop, which was absent in the apo-Kv1.3 map, can be seen in the dalazatide–Kv1.3 map. The Kvβ2 model contains 328 residues between R34 and S361. The VSD is in a depolarized conformation, and the S6 helical inner gate is open (*SI Appendix*, Fig. S21). Fig. 3*A* shows a dalazatide molecule bound to the extracellular side of Kv1.3's pore region, consistent with earlier electrophysiological, mutagenesis, and modeling studies (11, 14, 32). However, a model of dalazatide could not be built into its density most likely due to the symmetry mismatch arising from a nonsymmetrical dalazatide molecule binding to a fourfold symmetrical Kv1.3. Dalazatide can bind to any of four structurally identical but statistically different sites on the tetrameric channel in four possible orientations. In the averaged cryo-EM map, the dalazatide density likely represents a superposition of four individual orientations of dalazatide, each populated equally with one-fourth occupancy, with the density of each orientation reduced to one-fourth relative to the channel complex. Since dalazatide's density represents a minute fraction of the overall density in the cryo-EM map, we
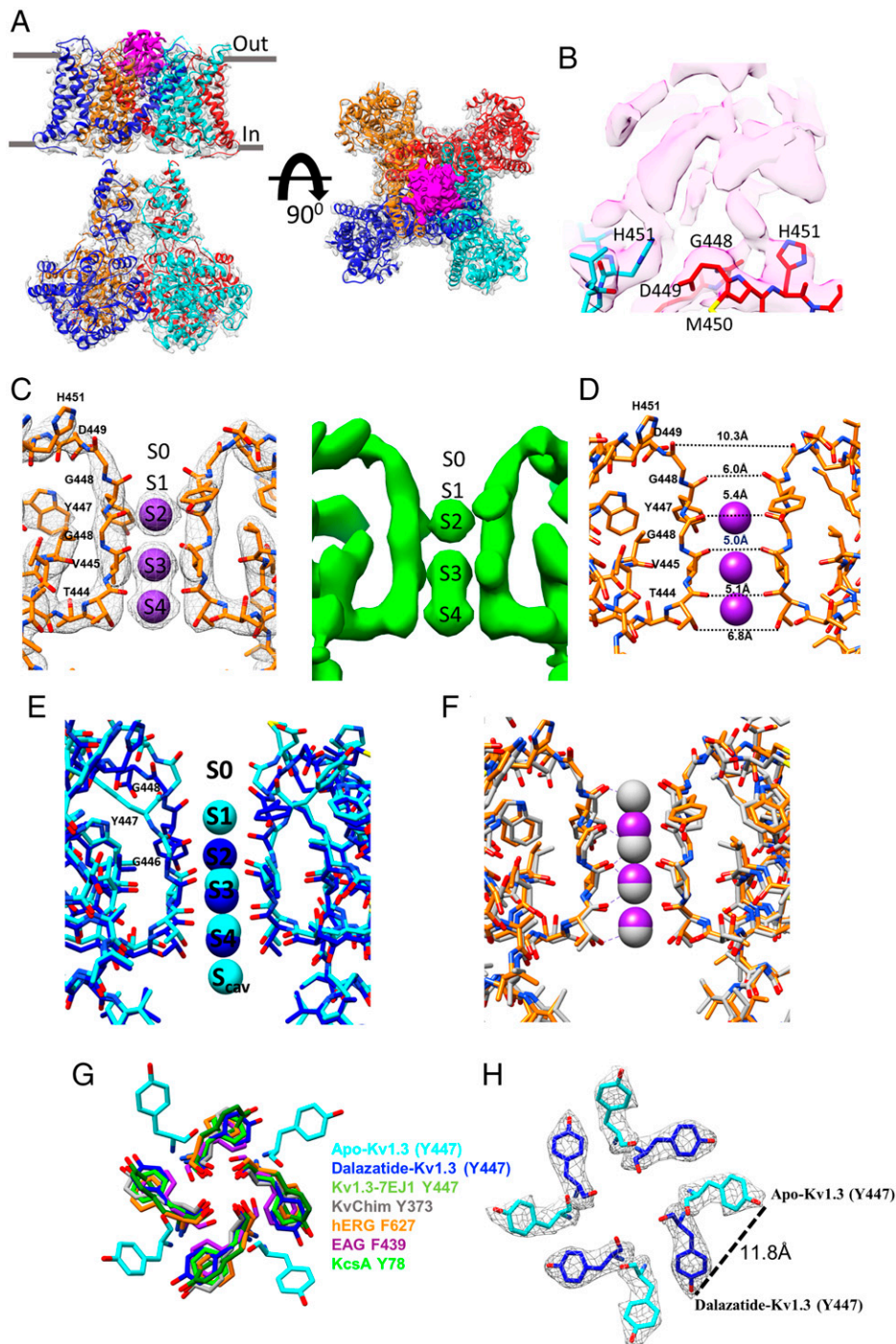
Fig. 3. Structure of dalazatide-bound human Kv1.3–Kvβ2 complex (dalazatide–Kv1.3). (*A*) Cryo-EM density map of dalazatide–Kv1.3 with fitted model viewed from the membrane plane (*Left*) and from the extracellular side (*Right*). (*B*) Dalazatide's interactions with G448 and H451 in Kv1.3's outer pore. The density around dalazatide is shown in magenta surface with the Kv1.3 model fitted. (*C*) Side view of EM density of the dalazatide–Kv1.3 map in white mesh with fitted model (*Left*) and surface in green (*Right*). (*D*) Distances between the carbonyl O atom of residues in the selectivity filter are shown. Only two opposite subunits are displayed for clarity. Residues in the selectivity filter are highlighted. K^+ ions (purple spheres) are seen at sites S2–S4; the K^+ ion is missing at site S1. (*E* and *F*) Comparison of the selectivity filter: dalazatide–Kv1.3 (dark blue) with apo-Kv1.3 (*E*) and dalazatide–Kv1.3 (orange) with KvChim (gray) (*F*). (*G*) Overlay of Y447 from apo-Kv1.3 (cyan) and dalazatide–Kv1.3 (dark blue) models with equivalent aromatic residues in the selectivity filters (shown as sticks) of Y373-KvChim (gray), F627-hERG (orange), F439-Eag-1 (purple), and Y78-KcsA (green). (*H*) Superposition of the EM density of Y447 in apo-Kv1.3 and dalazatide–Kv1.3 maps (gray mesh) with its fitted model. The position of Y447 varies by 11.8 Å in the two structures.

were unable to reduce this heterogeneity due to the lower signal-to-noise ratio of individual particles. Owing to these technical challenges, we were unable to build a model of dalazatide into its density and could identify only the most prominent interactions between dalazatide and Kv1.3. Both the C4 and C1 EM

density maps revealed a clear density for dalazatide in close proximity to residues (H451, M450, D449, and G448) in the outer pore (Fig. 3*B* and *SI Appendix*, Fig. S20C).

Dalazatide's interaction with Kv1.3 changes the architecture of the selectivity filter. Based on EM densities in the
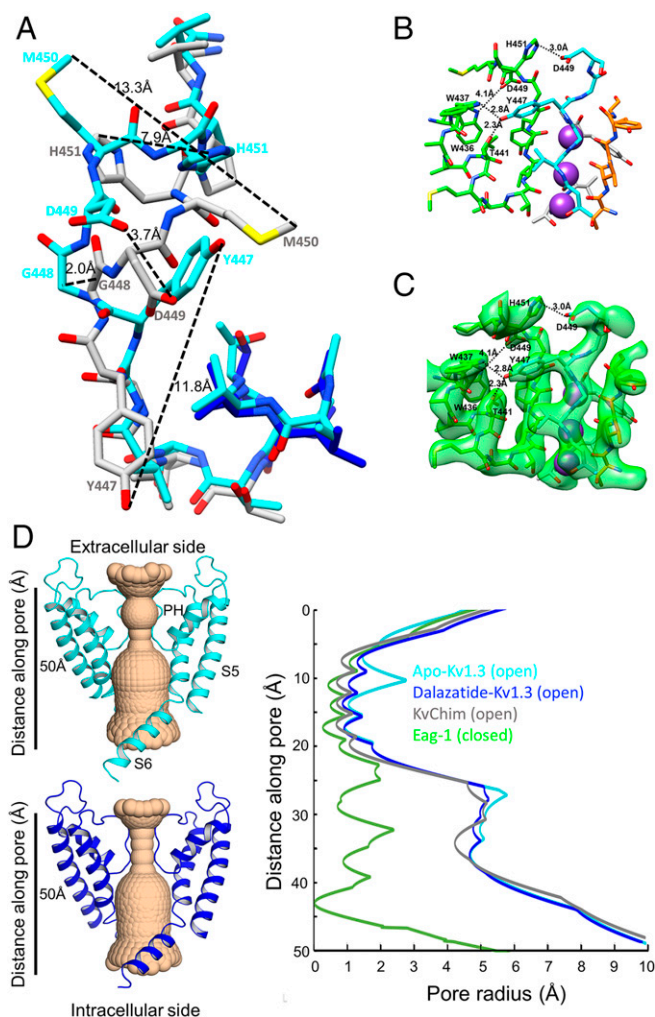
Fig. 4. Dalazatide-induced structural rearrangements in Kv1.3's selectivity filter. (*A*) Structural rearrangements in the selectivity filter of apo-Kv1.3 (cyan) and dalazatide–Kv1.3 (gray) show movement of Y447, G448, D449, M450, and H451 with distances moved depicted by dotted lines. (*B* and *C*) Model of the outer pore of Kv1.3 with individual subunits colored cyan, green, gray, and orange and shown as sticks (*B*) and with density in green (*C*). Distances are shown between W436 and D449 (4.1 Å) in the same subunit and W437 and Y447 (2.8 Å), T441 and Y447 (2.3 Å), and D449 and H451 (3.0 Å) in adjacent subunits. (*D*) The pore of apo-Kv1.3 (*Upper Left*) and dalazatide–Kv1.3 (*Lower Left*) generated with the "Hole" program is shown as a golden surface, and two opposite subunits are shown as ribbons. On the *Right*, the pore radii of apo-Kv1.3 (cyan) and dalazatide–Kv1.3 (blue) are plotted against distance from the extracellular surface. KvChim (gray; PDB: 2R9R) and Eag-1 (green; PDB: 5K7L) are included for comparison. The models were aligned using the IPDAFW-WAVVTMTTVGYG sequence.

dalazatide–Kv1.3 pore, we modeled K$^+$ ions at sites S2, S3, and S4, but site S1 was vacant (Fig. 3 *C* and *D* and *SI Appendix*, Fig. S20 *A* and *B*). The density observed over site S1 in both the C1 and C4 maps (*SI Appendix*, Fig. S20 *A* and *B*) may be a pore-occluding dalazatide residue. This pattern is similar to the crystal structure of charybdotoxin bound to KvChim, where K$^+$ ions were present at sites S2, S3, and S4, and the toxin's K27 projected straight into the pore and approached the top of an unoccupied site S1 (33). The selectivity filter of dalazatide–Kv1.3 (Fig. 3*C*), which is different from apo-Kv1.3, superimposes well with KvChim (Figs. 2*C* and 3 *E* and *F* and *SI Appendix*, Fig. S21 *A*–*D*). Relative to apo-Kv1.3, we see drastic shifts in the positions of Y447 (11.8 Å), G448 (2.0 Å), D449 (3.7 Å),

M450 (13.3 Å), and H451 (7.9 Å) (Fig. 4*A*). The new position of H451 weakens the H451–Y447 hydrogen bond, allowing Y447 to flip toward the interior of the selectivity filter where it superimposes well with corresponding aromatic residues in KvChim, hERG, Eag-1, and KcsA but differs significantly from apo-Kv1.3 (Fig. 3 *G* and *H*). In its new position, Y447 is close enough to W437 (2.8 Å) and T441 (2.3 Å) in the adjacent subunit to form intersubunit Y447–W437 and Y447–T441 hydrogen bonds (Fig. 4 *B* and *C*), similar to intersubunit hydrogen bonds that stabilize KvChim's outer pore (*SI Appendix*, Fig. S11*B*). The intrasubunit hydrogen bond (W436–D449) that prevents C-type inactivation (*SI Appendix*, Fig. S11*B*) is likely absent in dalazatide–Kv1.3 because the corresponding residues (W436 and D449) are more than 4 Å apart (Fig. 4 *B* and *C*). The absence of this intrasubunit hydrogen bond appears to be compensated by a new intersubunit hydrogen bond between D449 and H451 (3 Å) (Fig. 4 *B* and *C*). Thus, a network of three intersubunit hydrogen bonds (Y447–W437, Y447–T441, and H451–D449) may stabilize the selectivity filter of dalazatide–Kv1.3.

We compared the pore radii of apo-Kv1.3 and dalazatide–Kv1.3 generated using the "Hole" program (34) with the pores of KvChim and Eag-1 (Fig. 4*D*). The S6 helical inner gates of apo-Kv1.3, dalazatide–Kv1.3, and KvChim are open, while it is closed in Eag-1 (Fig. 4*D*). Despite the difference in the inner gate, the selectivity filters of dalazatide–Kv1.3, KvChim, and Eag-1 are similar in diameter, while the outer selectivity filter at site S2 of apo-Kv1.3 is widened (Fig. 4*D*). In summary, dalazatide binding to the outer pore vestibule region of Kv1.3 causes a dynamic rearrangement of the selectivity filter as the channel transitions from the unique selectivity filter conformation of apo-Kv1.3 to a peptide-blocked conformation.

MDS Studies. We performed all-atom MDS to assess ion-conducting properties of the pores of apo-Kv1.3 and dalazatide–Kv1.3 (with dalazatide removed) embedded in lipid bilayers in the presence of symmetric 150 mM KCl aqueous solution and a transmembrane voltage jump from 0 to 750 mV during 1-μs-long MDS runs. No restraints were applied to the protein during these simulations. For apo-Kv1.3, we observed rapid breaking of key intrasubunit hydrogen bonds (H451–Y447, H451–D449), leading to significant distortions of the outer selectivity filter and elimination of most K$^+$-binding sites with the exception of S3 and S4 (*SI Appendix*, Fig. S22 *A* and *C*). The selectivity filter at the level of G448, constricted in the cryo-EM structure, widened during the simulation and flooded with water. This resulted in a rapid stochastic outward permeation of K$^+$, during which ions were initially located in S3 and S4 and/or in between, in the plane of T444 carbonyl oxygens, and knocked on by incoming K$^+$ ions into the outer selectivity filter, where they got hydrated and left the pore (Movie S1). We observed 48 complete K$^+$ permeation events during the first 400 ns of the MDS under the applied voltage, resulting in the estimated conductance of ~26 pS. However, this observed process does not resemble conventional K$^+$-selective channel conduction and likely results from a structural instability of the apo-Kv1.3 structure under MDS conditions. This was confirmed by our MDS run of dalazatide–Kv1.3 (with dalazatide removed) under the same conditions.

Dalazatide–Kv1.3 demonstrated a much more stable selectivity filter structure and single-file knock-on K$^+$ conduction (*SI Appendix*, Fig. S22 *B* and *D* and Movie S2). We observed five complete K$^+$ conduction events during the first 23 ns of the MDS run under the applied 750-mV voltage, which is equivalent to ~46-pS single-channel conductance. However, after that, we saw long refractory periods and observed only three more K$^+$ conduction events in the remaining ~980 ns, resulting in a much lower estimate of conductance of just 1.7 pS from the whole 1-μs-long MDS with large uncertainty. While critical

Tyagi et al.
Rearrangement of a unique Kv1.3 selectivity filter conformation upon binding of a drug

PNAS | 7 of 10
https://doi.org/10.1073/pnas.2113536119

intersubunit W437–Y447 hydrogen bonds remain largely intact, T441–Y447 for one chain breaks after ~90 ns of the MDS under applied voltage. This correlates with transition of the Y447 backbone φ and side chain χ2 dihedral angles of this channel subunit from the initial gauche(−) orientation, which likely impedes effective selectivity filter ion conduction. We also observed slight narrowing of the inner gate during this MDS based on a ~1-Å decrease in the distances between C_α atoms of S6 residues P477, I472, and V469 on two opposite chains. This may also contribute to long refractory periods and thus reduced K^+ conduction. Interestingly, we also observed that intersubunit H451–D449 and intrasubunit W436–D449 hydrogen bonding interactions got broken for three of four chains, whereas intrasubunit H451–Y447 and H451–D449 hydrogen bonds, initially present in apo-Kv1.3, never formed during the MDS on dalazatide–Kv1.3. Additional simulations with different initial conditions, applied voltages, and simulation protocols are needed to further explore precise molecular mechanisms of ion conduction in this channel.

Conclusion

We used cryo-EM to determine structures of human Kv1.3 complexed to its accessory subunit Kvβ2 alone (apo-Kv1.3) and bound to dalazatide (dalazatide–Kv1.3), a peptide inhibitor in human trials. Both structures are in the activated state based on the depolarized voltage sensors and open S6 helical inner gate. In the apo-Kv1.3 structure, the outer pore is substantially rearranged compared to most other K^+ channels analyzed. The position of Y447 is drastically altered, being shifted 11 Å from that in other K^+ channels. The pore is widened at S1 and S2 but narrowed at S0. K^+ are present at S1, S3, and S4 but not S2. A network of intrasubunit hydrogen bonds (H451–Y447 and H451–D449) stabilizes this conformation. We propose that apo-Kv1.3 may be in the C-type inactivated conformation based on its structural features (widening of the selectivity filter at S2, lack of K^+ at S2, the absence of the critical intrasubunit hydrogen bond that prevents C-type inactivation, and similar conformation of the selectivity filter to that of W434F Shaker-IR, which has been suggested to be C-type inactivated) and its behavior during MDS (stochastic conduction of K^+ through an unstable outer selectivity filter during a voltage pulse after breakage of critical intrasubunit hydrogen bonds). Binding of dalazatide dramatically changes the unique conformation of Kv1.3's selectivity filter. The reordered filter of dalazatide–Kv1.3 is narrower than apo-Kv1.3, and ion-binding sites S2–S4 are occupied, while the density observed over S1 may be a pore-occluding dalazatide residue similar to the pore-occluding toxin residue seen in the charybdotoxin-bound structure of KvChim (33). This conformation is stabilized by a network of intersubunit hydrogen bonds (Y447–W437, Y447–T441, and H451–D449). Interestingly, the intrasubunit hydrogen bond (W436–D449) that prevents C-type inactivation (15) is likely absent. Note, Kv1.3 exhibits slow recovery from C-type inactivation, which underlies its unique property of cumulative or use-dependent inactivation. MDS of dalazatide–Kv1.3 (with dalazatide removed) shows that K^+ is conducted in single file through a stable selectivity filter during a voltage pulse. Our results highlight the usefulness of UT carbon films for cryo-EM studies to define the interaction of pharmacological modulators with Kv1.3 and to characterize Kv1.3 mutants with altered activation, inactivation, and use-dependent inactivation.

Materials and Methods

Cloning, Protein Expression, and Purification. DNA encoding human Kv1.3 (UniProtKB accession no. P22001), lacking the first 52 residues, and human Kvβ2.1(UniProtKB accession no. Q13303) were cloned for coexpression into a pFastBac dual vector (Invitrogen) with a FLAG tag (DYKDDDDK) at the amino

terminus of Kv1.3. Recombinant baculovirus expressing Kv1.3–Kvβ2.1 was generated using the Bac-to-Bac system (Invitrogen). For large-scale expression, baculovirus after two rounds of amplification was used to infect Sf9 cells at 2×10^6 cells/mL cultured in SIM SF Expression medium, for SF9 and SF21, Serum free (Sino Biological Inc.) at 27 °C. Infected Sf9 cells were cultured for 60 h before harvesting. The cell pellet from 1 L of culture was resuspended in lysis buffer (20 mM HEPES, pH 7.5, 150 mM KCl, and 10% glycerol). The suspension was supplemented with 1.5% (wt/vol) n-dodecyl-β-D-maltopyranoside (DDM; Anatrace), 0.3% (wt/vol) cholesteryl hemisuccinate (Sigma), and protease inhibitor mixture. After extraction at 4 °C for 2 h, the insoluble fraction was removed by ultracentrifugation at 180,000 × g for 45 min at 4 °C, and the supernatant was incubated with anti-FLAG M2 affinity gel (Sigma) at 4 °C. The resin was then collected and washed with wash (W) buffer (20 mM HEPES, pH 7.5, 150 mM KCl, and 0.1% GDN). The proteins were eluted with W buffer supplemented with 200 µg/mL FLAG peptide. After elution, the proteins were concentrated and further purified on a Superose 6 increase column (GE Healthcare) equilibrated with 20 mM HEPES, pH 7.5, 150 mM KCl, and 0.05% GDN. Peak fractions of the protein complex were concentrated to ~4 mg/mL, flash-frozen in liquid nitrogen, and stored at −80 °C.

Negative Staining EM. The Kv1.3–Kvβ2 complex was diluted to 0.025 mg/mL with 20 mM HEPES, pH 7.5, 150 mM KCl, and 0.05% GDN. Then, 3.5 µL of the diluted sample was applied to a freshly glow-discharged carbon-coated grid and stained with 2% uranyl acetate. EM images were recorded on an FEI T12 electron microscope with a 4K Eagle camera. Micrographs were processed with Relion3.1 to generate 2D class averages (19).

Cryo-EM Sample Preparation and Data Acquisition. The Kv1.3–Kvβ2 complex was diluted to 0.15 mg/mL with 20 mM HEPES, pH 7.5, 150 mM KCl, 0.05% GDN, and 0.01% LDAO. Then, 3.5 µL of protein sample was applied to freshly plasma-cleaned holey carbon grids (Quantifoil, R1.2/1.3, 300 mesh) with a homemade carbon support film. The grids were blotted for 2 to 3 s at 100% humidity and 8 °C with a Vitrobot Mark IV (Thermo Fisher Scientific) and plunge-frozen into liquid nitrogen-cooled liquid ethane. 1 µL of dalazatide (prepared in 20 mM HEPES, pH 7.5, 150 mM KCl, and 0.05% GDN) was directly added to 15 µL of Kv1.3–Kvβ2a (20 mM HEPES, pH 7.5, 150 mM KCl, 0.05% GDN, and 0.01% LDAO) to yield a 10× molar excess and incubated for 30 min on ice before freezing the grids for the dalazatide–Kv1.3 sample. The frozen grids were stored in liquid nitrogen until used. Grids were loaded onto a Titan Krios electron microscope (FEI) operated at 300 kV and equipped with a Gatan K3 direct detection camera. Images were recorded as movies in counting mode with a pixel size of 0.858 Å using the automated image acquisition software SerialEM (35). Movies were recorded as 50 frames in tagged image file format with a total dose of 65 electrons per Å².

Cryo-EM Data Processing. Movie frames were aligned with motion correction and dose weighting using University of California San Francisco (UCSF) MotionCor2 (36). Contrast transfer function (CTF) parameters were estimated with Gctf (37) using nondose-weighted micrographs. Particles were auto picked using the Laplacian function in Relion with 200- to 250-Å-sized particles. Extracted particles were subjected to multiple rounds of 2D classification to select good particles (*SI Appendix*, Figs. S4 and S14). First, four rounds of 2D classification were performed at 5× binned particles followed by four rounds each at 3× and 2× binning. Ten thousand particles from good class averages were used to generate an initial model de novo using the stochastic gradient descent algorithm in Relion. A 60-Å low-pass filtered initial model was used as a reference for 3D classification into ten classes at 2× binned particles. Good 3D classes were combined and repeated multiple times to obtain a homogeneous set of particles.

A total of 321,674 particles of the apo-Kv1.3 data set were subjected to 3D autorefinement in Relion, which yielded a 3D EM density map of the entire Kv1.3–Kvβ2.1 complex resolved to a 3.1-Å resolution after CTF refinement and particle polishing. Using signal subtraction of the transmembrane region from the particle and only focusing on the soluble domain, a 3D density map was obtained and resolved to a 2.9-Å resolution with C4 symmetry applied. Signals of the soluble region were subtracted from the original particles, and we focused on the transmembrane domain. Following 2D and 3D classifications and 3D refinement of 177,130 particles, we obtained a 3D map resolved to 3.4- and 3.9-Å resolution with C4 and C1 symmetry applied. Autorefinement of 363,241 particles of dalazatide–Kv1.3 yielded a 3D EM density map of the entire drug-bound Kv1.3–Kvβ2.1 complex (dalazatide–Kv1.3) resolved to 2.9-Å resolution, which could be further improved to 2.7 Å. After signal subtraction of the soluble region from the original particles and by focusing on the transmembrane domain followed by 2D and 3D classifications and 3D refinement of 153,218 particles, we obtained a 3D density map resolved to

3.4- and 3.7-Å resolution with C4 and C1 symmetry applied. Resolutions of the transmembrane regions were estimated by applying a soft mask excluding detergent micelle and the gold standard Fourier shell correlation (FSC) using the 0.143 criterion. Local resolution was determined using ResMap in Relion (38) with unfiltered maps as input maps.

Model Building. The coordinates of PDB entry 2R9R of KvChim (20) were used to build the Kv1.3 models. Initially, 2R9R was a rigid body docked in the focused maps obtained by cryo-EM for the transmembrane and tetramerization domains and the Kvβ2 subunits. Thereafter, phenix.real_space_refine (39) was used along with the secondary structure and noncrystallographic symmetry (NCS) restraints to improve the fit of the models, which was then manually rebuilt in COOT (40). For the four NADP$^+$ cofactors that bind Kvβ2, restraints were generated using the eLBOW (41) tool from the PHENIX software package and used during refinement. Models for phospholipid molecules, cholesteryl hemisuccinate, and 12 acyl tails that copurify with the protein were built by visual inspection of the shape of the densities, and restraints were similarly generated and used during refinement. Densities for water molecules and K$^+$ ions were modeled in COOT, which were then combined with the rest of the model and refined using phenix.real_space_refine.

Model Validation. The atomic models of Kv1.3 were validated using the Molprobity server (42). Model overfitting was estimated from the FSC curves between cryo-EM maps and models. To obtain these FSC curves, all frequencies until Nyquist were taken to generate simulated maps from the final models and then resampled onto the same grid as the cryo-EM maps in UCSF Chimera (43). Thereafter, FSC values were obtained using the e2proc3d.py program in EMAN 2.31 (44). Local agreement between maps and models was calculated using the "vop localCorrelation" command in UCSF Chimera. Details about the model validation and refinement statistics are provided in *SI Appendix*, Table S1.

Electrophysiology. Dalazatide was purchased from Alomone Labs (Jerusalem, Israel). The effects of dalazatide on Kv1.3 were evaluated by whole-cell patch clamp using a QPatch HTX automated electrophysiology platform (Sophion Biosciences) using L929 cells stably expressing the Kv1.3 channel (45). Dalazatide was prepared as 0.1 mM stock solutions in P6N buffer (10 mM sodium phosphate, 0.8% [wt/vol] NaCl, and 0.05% [vol/vol] Tween 20, pH 6) and diluted with 0.1% (wt/vol) bovine serum albumin in external buffer. The gigaseal and whole-cell requirements for the automated electrophysiology were as follows: minimum seal resistance of 0.1 GΩ, holding potential of −90 mV, holding pressure of 20 mbar, and positioning pressure of −70 mbar. Kv1.3 currents were elicited by 50-, 200-, 1,000-, or 2,000-ms depolarizing pulses to 40 mV from the holding potential of −80 mV. The interpulse interval was 45 s to avoid cumulative inactivation. The external solution was comprised of the following: 4.5 mM KCl, 160 mM NaCl, 1 mM MgCl$_2$, 2 mM CaCl$_2$, and 10 mM HEPES, pH 7.2. The internal buffer was composed of 160 mM KF, 2 mM MgCl$_2$, 10 mM egtazic acid, and 10 mM HEPES, pH 7.2. The amplitudes of the peak current and steady-state current and inactivation time constant (τ_h) were measured using the Sophion QPatch software 5.6 and exported to GraphPad Prism 9 for analysis.

MDS. We used atomistic structural models of the apo-Kv1.3 and dalazatide–Kv1.3 (with dalazatide removed) membrane-spanning pore and voltage-sensing domains (residues 208 to 493 or 490, respectively). Standard up-to-date all-atom CHARMM force fields for proteins (46), lipids (47), ions, and the transferable intermolecular potential with 3 points (TIP3P) water model were used. Kv1.3 channel models were embedded in a 1-palmitoyl-2-oleoylphosphatidylcholine (POPC) bilayer and solvated by 0.15 M aqueous KCl solution using CHARMM-GUI, resulting in a 156-K atom systems with periodic boundary conditions. These were equilibrated with the NAMD program in maintaining constant number of particles, pressure, and temperature (NPT) ensemble at 310 K and 1 atm pressure for 90 ns using a staged MDS protocol with gradually reduced restraints during the first 40 ns (48). Those runs were followed by unrestrained 1-μs-long MDS on Anton 2 (49) under the 750-mV applied transmembrane voltage in the *NVT* ensemble using standard simulation parameters as was done previously (50). Simulation trajectories were analyzed using the VMD program.

1. S. P. Alexander *et al.*, The concise guide to pharmacology 2017/18: Voltage-gated ion channels. *Br. J. Pharmacol.* **174** (suppl. 1), S160–S194 (2017).
2. S. Bernèche, B. Roux, A gate in the selectivity filter of potassium channels. *Structure* **13**, 591–600 (2005).
3. D. A. Doyle *et al.*, The structure of the potassium channel: Molecular basis of K$^+$ conduction and selectivity. *Science* **280**, 69–77 (1998).
4. J. H. Morais-Cabral, Y. Zhou, R. MacKinnon, Energetic optimization of ion conduction rate by the K$^+$ selectivity filter. *Nature* **414**, 37–42 (2001).
5. Y. Zhou, J. H. Morais-Cabral, A. Kaufman, R. MacKinnon, Chemistry of ion coordination and hydration revealed by a K$^+$ channel-Fab complex at 2.0 Å resolution. *Nature* **414**, 43–48 (2001).
6. J. F. Cordero-Morales *et al.*, Molecular determinants of gating at the potassium-channel selectivity filter. *Nat. Struct. Mol. Biol.* **13**, 311–318 (2006).
7. L. Heginbotham, Z. Lu, T. Abramson, R. MacKinnon, Mutations in the K$^+$ channel signature sequence. *Biophys. J.* **66**, 1061–1067 (1994).
8. W. Wang, R. MacKinnon, Cryo-EM structure of the open human ether-à-go-go-related K$^+$ channel hERG. *Cell* **169**, 422–430 (2017).
9. M. D. Cahalan, K. G. Chandy, The functional network of ion channels in T lymphocytes. *Immunol. Rev.* **231**, 59–87 (2009).
10. H. Wulff, P. Christophersen, P. Colussi, K. G. Chandy, V. Yarov-Yarovoy, Antibodies and venom peptides: New modalities for ion channels. *Nat. Rev. Drug Discov.* **18**, 339–357 (2019).
11. K. G. Chandy, R. S. Norton, Peptide blockers of K$_v$1.3 channels in T cells as therapeutics for autoimmune disease. *Curr. Opin. Chem. Biol.* **38**, 97–107 (2017).
12. E. J. Tarcha *et al.*, Durable pharmacological responses from the peptide ShK-186, a specific Kv1.3 channel inhibitor that suppresses T cell mediators of autoimmune disease. *J. Pharmacol. Exp. Ther.* **342**, 642–653 (2012).
13. E. J. Tarcha *et al.*, Safety and pharmacodynamics of dalazatide, a Kv1.3 channel inhibitor, in the treatment of plaque psoriasis: A randomized phase 1b trial. *PLoS One* **12**, e0180762 (2017).
14. M. W. Pennington *et al.*, Engineering a stable and selective peptide blocker of the Kv1.3 channel in T lymphocytes. *Mol. Pharmacol.* **75**, 762–773 (2009).
15. S. A. Pless, J. D. Galpin, A. P. Niciforovic, H. T. Kurata, C. A. Ahern, Hydrogen bonds as molecular timers for slow inactivation in voltage-gated potassium channels. *eLife* **2**, e01289 (2013).
16. S. Liu *et al.*, Structures of wild-type and H451N mutant human lymphocyte potassium channel K$_v$1.3. *Cell Discov.* **7**, 39 (2021).
17. Y. C. Cai, P. B. Osborne, R. A. North, D. C. Dooley, J. Douglass, Characterization and functional expression of genomic DNA encoding the human lymphocyte type n potassium channel. *DNA Cell Biol.* **11**, 163–172 (1992).
18. S. Grissmer *et al.*, Expression and chromosomal localization of a lymphocyte K$^+$ channel gene. *Proc. Natl. Acad. Sci. U.S.A.* **87**, 9411–9415 (1990).
19. J. Zivanov *et al.*, New tools for automated high-resolution cryo-EM structure determination in RELION-3. *eLife* **7**, e42166 (2018).
20. S. B. Long, X. Tao, E. B. Campbell, R. MacKinnon, Atomic structure of a voltage-dependent K$^+$ channel in a lipid membrane-like environment. *Nature* **450**, 376–382 (2007).
21. J. R. Whicher, R. MacKinnon, Structure of the voltage-gated K$^+$ channel Eag1 reveals an alternative voltage sensing mechanism. *Science* **353**, 664–669 (2016).
22. D. Matthies *et al.*, Single-particle cryo-EM structure of a voltage-activated potassium channel in lipid nanodiscs. *eLife* **7**, e37558 (2018).
23. A. E. Busch, R. S. Hurst, R. A. North, J. P. Adelman, M. P. Kavanaugh, Current inactivation involves a histidine residue in the pore of the rat lymphocyte potassium channel RGK5. *Biochem. Biophys. Res. Commun.* **179**, 1384–1390 (1991).
24. A. Nguyen *et al.*, Novel nonpeptide agents potently block the C-type inactivated conformation of Kv1.3 and suppress T cell activation. *Mol. Pharmacol.* **50**, 1672–1679 (1996).
25. S. Somodi *et al.*, pH-dependent modulation of Kv1.3 inactivation: Role of His399. *Am. J. Physiol. Cell Physiol.* **287**, C1067–C1076 (2004).
26. J. F. Cordero-Morales, V. Jogini, S. Chakrapani, E. Perozo, A multipoint hydrogen-bond network underlying KcsA C-type inactivation. *Biophys. J.* **100**, 2387–2393 (2011).

Tyagi et al.
Rearrangement of a unique Kv1.3 selectivity filter conformation upon binding of a drug

PNAS | 9 of 10
https://doi.org/10.1073/pnas.2113536119

27. J. D. Lueck et al., Atomic mutagenesis in ion channels with engineered stoichiometry. eLife **5**, e18976 (2016).

28. X.-F. Tan et al., Structure of the Shaker Kv channel and mechanism of slow C-type inactivation. bioRxiv [Preprint] (2021). https://doi.org/10.1101/2021.09.21.461258 (Accessed 21 September 2021).

29. A. Lange et al., Toxin-induced conformational changes in a potassium channel revealed by solid-state NMR. Nature **440**, 959–962 (2006).

30. U. Zachariae et al., The molecular mechanism of toxin-induced conformational changes in a potassium channel: Relation to C-type inactivation. Structure **16**, 747–754 (2008).

31. C. Oliva, V. González, D. Naranjo, Slow inactivation in voltage gated potassium channels is insensitive to the binding of pore occluding peptide toxins. Biophys. J. **89**, 1009–1019 (2005).

32. S. C. Chang et al., N-Terminally extended analogues of the K+ channel toxin from Stichodactyla helianthus as potent and selective blockers of the voltage-gated potassium channel Kv1.3. FEBS J. **282**, 2247–2259 (2015).

33. A. Banerjee, A. Lee, E. Campbell, R. Mackinnon, Structure of a pore-blocking toxin in complex with a eukaryotic voltage-dependent K+ channel. eLife **2**, e00594 (2013).

34. O. S. Smart, J. G. Neduvelil, X. Wang, B. A. Wallace, M. S. Sansom, HOLE: A program for the analysis of the pore dimensions of ion channel structural models. J. Mol. Graph. **14**, 354–360, 376 (1996).

35. D. N. Mastronarde, Serial EM: A program for automated tilt series acquisition on Tecnai microscopes using prediction of specimen position. Microsc. Microanal. **9**, 1182–1183 (2003).

36. S. Q. Zheng et al., MotionCor2: Anisotropic correction of beam-induced motion for improved cryo-electron microscopy. Nat. Methods **14**, 331–332 (2017).

37. K. Zhang, Gctf: Real-time CTF determination and correction. J. Struct. Biol. **193**, 1–12 (2016).

38. A. Kucukelbir, F. J. Sigworth, H. D. Tagare, Quantifying the local resolution of cryo-EM density maps. Nat. Methods **11**, 63–65 (2014).

39. P. D. Adams et al., PHENIX: A comprehensive Python-based system for macromolecular structure solution. Acta Crystallogr. D Biol. Crystallogr. **66**, 213–221 (2010).

40. P. Emsley, B. Lohkamp, W. G. Scott, K. Cowtan, Features and development of Coot. Acta Crystallogr. D Biol. Crystallogr. **66**, 486–501 (2010).

41. N. W. Moriarty, R. W. Grosse-Kunstleve, P. D. Adams, electronic Ligand Builder and Optimization Workbench (eLBOW): A tool for ligand coordinate and restraint generation. Acta Crystallogr. D Biol. Crystallogr. **65**, 1074–1080 (2009).

42. C. J. Williams et al., MolProbity: More and better reference data for improved all-atom structure validation. Protein Sci. **27**, 293–315 (2018).

43. E. F. Pettersen et al., UCSF Chimera–A visualization system for exploratory research and analysis. J. Comput. Chem. **25**, 1605–1612 (2004).

44. S. J. Ludtke, 3-D structures of macromolecules using single-particle analysis in EMAN. Methods Mol. Biol. **673**, 157–173 (2010).

45. S. Grissmer et al., Pharmacological characterization of five cloned voltage-gated K+ channels, types Kv1.1, 1.2, 1.3, 1.5, and 3.1, stably expressed in mammalian cell lines. Mol. Pharmacol. **45**, 1227–1234 (1994).

46. J. Huang et al., CHARMM36m: An improved force field for folded and intrinsically disordered proteins. Nat. Methods **14**, 71–73 (2017).

47. J. B. Klauda et al., Update of the CHARMM all-atom additive force field for lipids: Validation on six lipid types. J. Phys. Chem. B **114**, 7830–7843 (2010).

48. K. R. DeMarco et al., Atomistic modeling towards predictive cardiotoxicity. bioRxiv [Preprint] (2019). https://doi.org/10.1101/635441 (Accessed 11 May 2019).

49. D. E. Shaw et al., "Anton 2: Raising the bar for performance and programmability in a special-purpose molecular dynamics supercomputer" in SC14: International Conference for High Performance Computing, Networking, Storage and Analysis, pp. 41–53 (2014).

50. W. E. Miranda et al., Selectivity filter modalities and rapid inactivation of the hERG1 channel. Proc. Natl. Acad. Sci. U.S.A. **117**, 2795–2804 (2020).